

Radial variation of the stellar mass functions in the globular clusters M15 and M30: clues of a non-standard IMF?

M. Cadelano^{1,2*}, E. Dalessandro², J. J. Webb³, E. Vesperini⁴, D. Lattanzio¹, G. Beccari⁵,
M. Gomez⁶ and L. Monaco⁶

¹*Dipartimento di Fisica e Astronomia, Via Gobetti 93/2 I-40129 Bologna, Italy*

²*INAF-Astrophysics and Space Science Observatory Bologna, Via Gobetti 93/3 I-40129 Bologna, Italy*

³*Department of Astronomy and Astrophysics, University of Toronto, 50 St. George Street, Toronto ON M5S 3H4, Canada*

⁴*Department of Astronomy, Indiana University, Swain West, 727 E. 3rd Street, Bloomington, IN 47405, USA*

⁵*European Southern Observatory, Karl-Schwarzschild-Strasse 2, 85748 Garching bei Munchen*

⁶*Departamento de Ciencias FÁsicas, Universidad Andres Bello, Republica 220, 837-0134 Santiago, Chile.*

Accepted XXX. Received YYY; in original form ZZZ

ABSTRACT

We exploit a combination of high-resolution *Hubble Space Telescope* and wide-field *ESO-VLT* observations to study the slope of the global mass function (α_G) and its radial variation ($\alpha(r)$) in the two dense, massive and post core-collapse globular clusters M15 and M30. The available data-set samples the clusters' Main Sequence down to $\sim 0.2 M_\odot$ and the photometric completeness allows the study of the mass function between $0.40 M_\odot$ and $0.75 M_\odot$ from the central regions out to their tidal radii. We find that both clusters show a very similar variation in $\alpha(r)$ as a function of cluster-centric distance. They both exhibit a very steep variation in $\alpha(r)$ in the central regions, which then attains almost constant values in the outskirts. Such a behavior can be interpreted as the result of long-term dynamical evolution of the systems driven by mass-segregation and mass-loss processes. We compare these results with a set of direct N -body simulations and find that they are only able to reproduce the observed values of $\alpha(r)$ and α_G at dynamical ages (t/t_{rh}) significantly larger than those derived from the observed properties of both clusters. We investigate possible physical mechanisms responsible for such a discrepancy and argue that both clusters might be born with a non-standard (flatter/bottom-lighter) initial mass function.

Key words: globular clusters: individual - Galaxy: kinematics and dynamics - galaxies: star clusters: general

1 INTRODUCTION

Globular clusters (GCs) are among the most populous, old, and dense stellar aggregates in the Universe and they play a crucial role in the study of many aspects of stellar evolution, stellar dynamics, and the interplay between these two aspects (see e.g. [Heggie & Hut 2003](#)).

After an initial evolutionary phase likely driven by cluster environmental properties and stellar evolution, mainly related to high-mass star mass-loss and supernovae explosions (see, e.g. [Gieles et al. 2006](#); [Kruijssen et al. 2011, 2012](#); [Renaud & Gieles 2013](#); [Rieder et al. 2013](#); [Mamikonyan et al. 2017](#); [Li & Gnedin 2019](#)), the long-term dynamical evolution of a GC is driven by two-body relaxation and the

external tidal field (see e.g. [Heggie & Hut 2003](#) and references therein). The effects of two-body relaxation drive more massive stars toward the cluster's center (mass segregation), while less massive stars migrate toward the cluster's outer regions. At the same time, this effect causes some stars to increase their energy and eventually escape the cluster.

The typical timescale associated with the effects of two-body relaxation is of the order of $1 - 2$ Gyr for most GCs ([Meylan, & Heggie 1997](#)), which is significantly shorter than the average age of Galactic GCs (~ 12 Gyr), thus suggesting that most of them have experienced quite a significant evolution. The internal dynamics of stellar aggregates affect objects of any mass and its effects have been often probed by means of massive test stars, like blue straggler stars, binaries and millisecond pulsars (e.g. [Ferraro et al. 2012, 2018](#);

* E-mail: mario.cadelano@unibo.it

Lanzoni et al. 2007, 2016; Dalessandro et al. 2009, 2011; Cadelano et al. 2015, 2018, 2019).

The effects of mass segregation have also been traced by studying the radial variation of the slope of the stellar mass function (MF; Beccari et al. 2011; Dalessandro et al. 2015; Webb et al. 2017). In fact, the combined effects of mass segregation and star loss leads to the formation of gradients in the local (i.e. measured at different clustercentric distances) MF and to a gradual flattening of the global MF (e.g. Vesperini & Heggie 1997; Baumgardt & Makino 2003; Webb & Vesperini 2016). The effects of internal dynamics on variations in the local and the global MFs therefore need to be carefully considered in the interpretation of the observed differences between the MFs of various GCs. Interestingly, by means of detailed comparison between observations and N -body models, we have shown (Webb & Vesperini 2016; Webb et al. 2017) that the combined measurements of the internal radial variation in the slope of the MF (δ_α) and its global value (α_G) are able not only to trace the long-term dynamical evolution of a cluster, but also to put critical constraints on the system's initial MF (IMF). This constraint is of critical importance, as the IMF influences most of the observable properties (e.g. chemical composition, mass-to-light-ratio) of any stellar system, from star clusters to galaxies. Hence detecting variations in the IMF can provide deep insight into the processes by which stars form. While significant efforts have been made to study the IMF in a variety of different environments, no consensus has been reached regarding its universality (e.g. Strader et al. 2011; Shanahan & Gieles 2015).

As a part of a large program aimed at constraining the degree of dynamical evolution of GCs by analyzing their MF radial variations and studying possible variations of their IMFs (Dalessandro et al. 2015; Webb et al. 2017), here we present a detailed study of the MF of two dynamically evolved globular clusters: M15 (NGC7078) and M30 (NGC7099). Both clusters orbit the Galactic halo and have quite similar structural properties. They are both dense ($\log \rho_c (M_\odot/\text{pc}^3) \sim 7.5$ and ~ 5.9 for M15 and M30, respectively) and relatively massive systems ($\sim 10^5 M_\odot$; Baumgardt, & Hilker 2018), hosting a stellar population with a very similar metallicity ($[Fe/H] \sim -2.3$; Carretta et al. 2009; Lovisi et al. 2013) and age (~ 13.25 Gyr, Dotter et al. 2010). Table 1 summarizes the main properties of the two systems. Based on the analysis of their blue straggler stars radial distribution (Ferraro et al. 2012, 2018; Lanzoni et al. 2016; Beccari et al. 2019) both clusters appears to be dynamically very old. In addition, studies of the density profiles (Noyola & Gebhardt 2006; Ferraro et al. 2009, Beccari et al., in prep.) show that both clusters have already experienced core collapse. Undergoing core-collapse is another indication that these clusters are in advanced evolutionary stages and that their local and global MFs may have been significantly affected by evolutionary processes. Along the same line, in both clusters a double blue straggler star sequence has been observed (Ferraro et al. 2009; Beccari et al. 2019). Such a feature, which has been detected in several clusters now (namely M30, M15, NGC362 and possibly NGC1261; Ferraro et al. 2009; Dalessandro et al. 2013; Simunovic et al. 2014; Beccari et al. 2019) is interpreted as a clear indication of a quite advanced dynamical stage possibly connected with the core-collapse event.

Table 1. Main properties of the two clusters analyzed in this work. From top to bottom: mass, 2D half-mass and tidal radii, log of the central density, age, metallicity and log of the half-mass relaxation time.

Param.	M15	M30	Ref.
M ($10^5 M_\odot$)	4.99 ± 0.05	1.39 ± 0.06	B19
r_{hm} (")	78 ± 8	92 ± 9	B20,F09
r_t (")	750	850	B20,F09
D (Kpc)	10.22 ± 0.13	8.0 ± 0.6	B19
$\log \rho_c$ ($M_\odot \text{pc}^{-3}$)	7.5	5.9	B19
Age (Gyr)	13.25 ± 0.75	13.25 ± 0.75	D10
$[Fe/H]$	-2.3	-2.3	C09,L13
$\log t_{rh}$ (yr)	9.39 ± 0.08	9.11 ± 0.09	This work

References: B19 (Baumgardt et al. 2019); B20 (Beccari et al., in prep.); F09 (Ferraro et al. 2009); D10 (Dotter et al. 2010); C09 (Carretta et al. 2009); L13 (Lovisi et al. 2013).

The outline of the paper is the following: in Section 2 we present the data-set, the data reduction and artificial star test. Section 3 reports on the MFs of the two clusters and their radial variation. In Section 4 we compare the observational results with a set of N -body models. Finally, in Section 5 we draw our conclusions.

2 OBSERVATIONS AND DATA ANALYSIS

To study the radial variation of the MF along the entire cluster with adequate spatial resolution and photometric completeness, we combined high-resolution Hubble Space Telescope (HST) data with wide-field ground-based photometry. For M30 and M15 we made use of two twin data-sets and data-reduction strategies.

To sample the cluster's innermost and crowded regions we used the publicly available catalogs obtained as a part of the *ACS Treasury Survey of Galactic Globular Clusters* (Sarajedini et al. 2007). The survey was performed by using observations acquired with the Advanced Camera for Surveys aboard HST (proposal GO 10775; P.I.: Sarajedini). The data-set are composed of images equally split between the F606W and F814W bands and obtained with a combination of long and short exposure times (see Sarajedini et al. 2007; Anderson et al. 2008 for details). The catalogs also provide calibrated Johnson V-band and I-band magnitudes, which we adopted throughout the whole work for homogeneity purposes with the wide-field catalogs. These images approximately sample the cluster's extension till their half-mass radii (see Table 1).

The ground-based wide-field data-set samples each cluster's outer regions out to their tidal radii and consists of images acquired with the VIMOS camera mounted on the UT3 (Melipal) telescope at Paranal VLT/ESO observatory under Program ID: 097.D-0145(A) (PI: Dalessandro). In the case of M15, the data-set is composed of 12 images obtained with the Johnson V filter with exposure times of 305 s and 12 images obtained with the Johnson I filter with exposure times of 280 s. The images sample two overlapping fields of view (see Figure 1), the first one centered at about $500''$ west from the cluster center and the second one at about $1250''$ west from the cluster. In the case of M30, the data-set is composed of 16 images per filter and we adopted the same combination of filters, exposure times and field of view

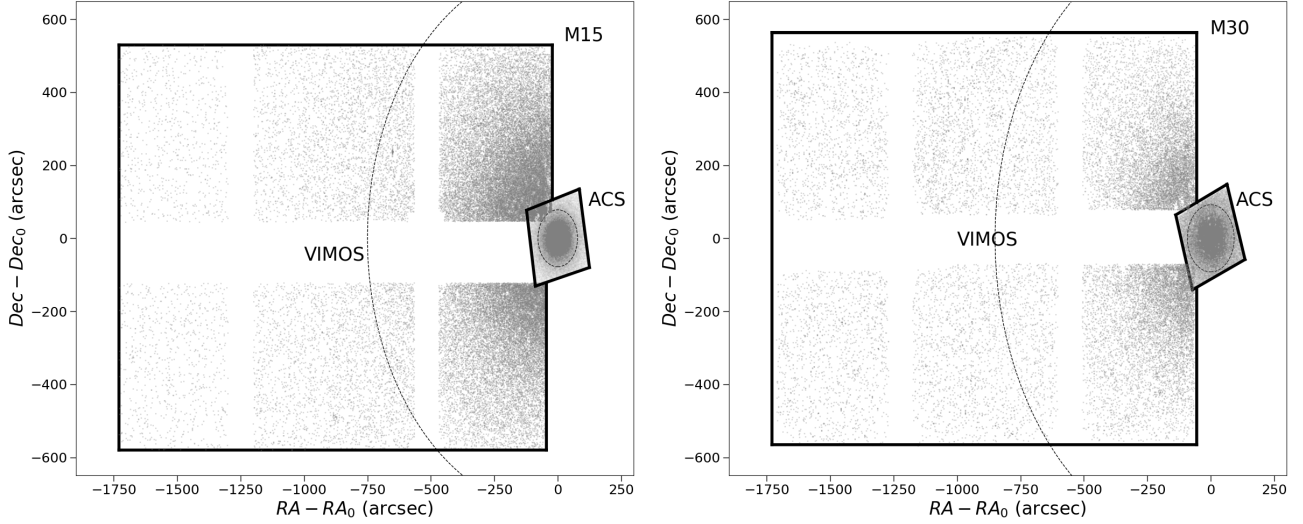


Figure 1. Field of views covered by the observations used in this work for M15 (left panel) and M30 (right panel). Each point represents a star. White regions without stars correspond to the inter-chip gaps of the VIMOS detector. The inner and outer dashed circles are the cluster’s projected half-mass and tidal radii, respectively (see Table 1).

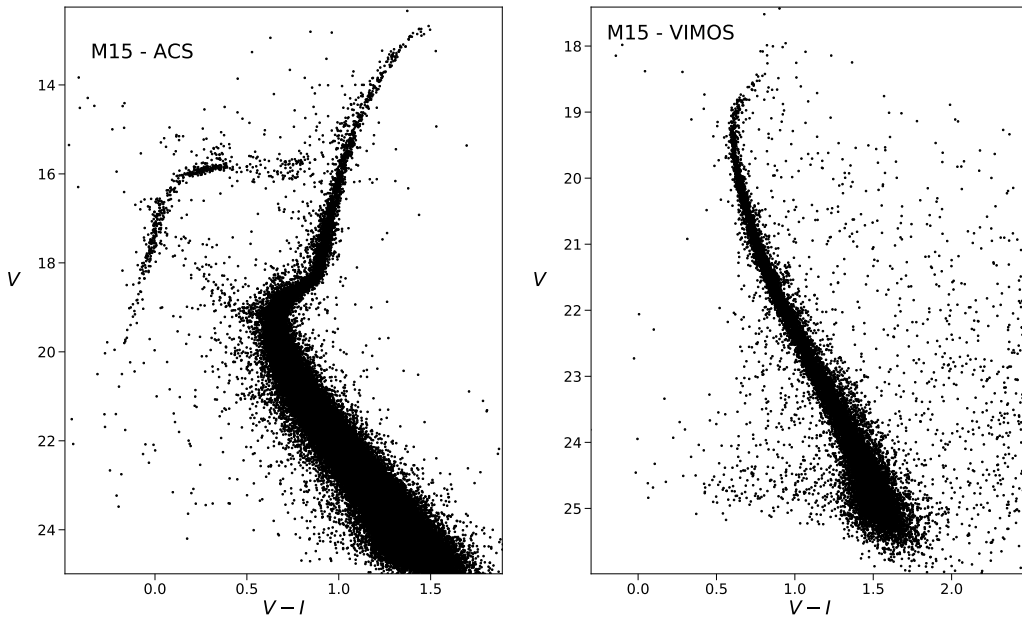


Figure 2. *Left panel:* V vs $(V - I)$ CMD of M15 as obtained from the high-resolution HST data-set by (Sarajedini et al. 2007). *Right panel:* V vs $(V - I)$ CMD of M15 as obtained from the ground based and wide field VIMOS data-set.

coverage. The resulting total field of views extend beyond each cluster’s tidal radii.

For each cluster, after correcting the images for bias and flat-field, we performed the photometric analysis independently on each image and on each chip of the detector by using DAOPHOT IV (Stetson 1987). As a first step, an adequate number of bright but not saturated stars have been chosen to model the point-spread function in each frame. This function was then applied to all the sources detected at 4σ above the background. We then created a master-list including all the sources detected in at least half of the images of each chip and, finally, a fit was forced in all the frames at

the corresponding positions using DAOPHOT/ALLFRAME (Stetson 1994). For each star of the resulting catalog, we homogenized the magnitudes measured in different images and their weighted means and standard deviations have been adopted as the star’s final magnitude and its related uncertainty. The instrumental positions have been transformed to the absolute system by using the stars in common with the Gaia Data Release 2 archive (Gaia Collaboration et al. 2018). The instrumental magnitudes have been reported to the Johnson photometric system by using the stars in common with the wide-field catalog described by Stetson et al.

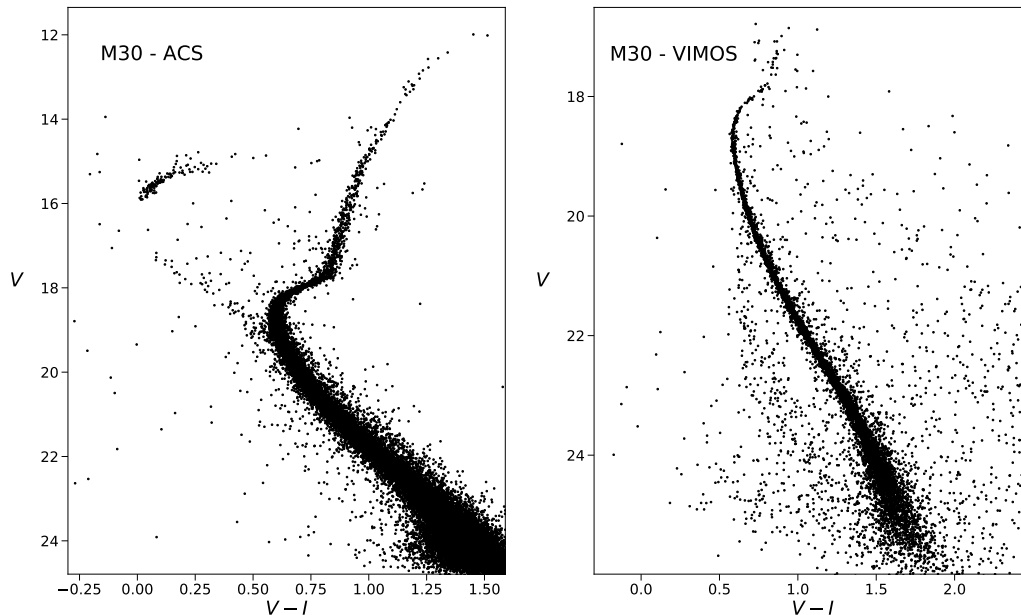


Figure 3. As in Figure 2, but for the M30 data-set.

(2019) and Ferraro et al. (2009) for M15 and M30, respectively.

The total field of view covered by both the high resolution and wide field data-sets is shown in Figure 1, while the obtained color-magnitude diagrams (CMDs) are plotted in Figure 2 and Figure 3.

2.1 Artificial star test

To study the MF of the clusters and its radial variation it is necessary to take into account the completeness level of our catalogs for stars with different magnitudes and located at different distances from the cluster centers. To this aim, we run artificial star experiments. For the ACS data-set, we used the artificial star catalogs provided along with the main catalogs of the *ACS Survey of Galactic Globular Clusters* (see Section 6 of Anderson et al. 2008).

For the VIMOS data-set, we performed a large number of artificial star experiments following the prescriptions described in Dalessandro et al. 2015 (see also Bellazzini et al. 2002). We created a list of artificial stars with a V-band input magnitude extracted from a luminosity function modeled to reproduce the observed ones in the same filters and extrapolated beyond the limiting magnitude. Then, to each of these stars, we assigned an I-band magnitude by interpolating along the mean ridge line of the clusters. These artificial stars were added to the real images by using the DAOPHOT/ADDSTAR software. The photometric reduction process and the point-spread function models used for the artificial star experiments are exactly the same as described in Section 2. This process was iterated multiple times and, in order to avoid “artificial crowding”, stars were placed into the frames in a regular grid composed of 38×38 pixel cells (corresponding approximately to ten times the typical FWHM of the point spread function) in which only one artificial star for each run was allowed to lie. At the end of the

runs, about 100000 and 150000 were simulated for the entire field of view covered by the M15 and M30 VIMOS data-set, respectively.

A completeness value $C = N_o/N_i$, defined as the ratio between the number of stars recovered at the end of the artificial star test (N_o) and that of stars actually simulated (N_i), was assigned to each star by using the following approach. To account for the effect of crowding (and therefore of the distance of the stars from the cluster center) on the completeness, for each star the completeness C was derived by using only objects located within a radial bin centered on the location of the star and with a width of $5''$ and $50''$ for the ACS and VIMOS data-sets, respectively. The bin widths were chosen as a compromise between having enough statistics and sampling a limited radial extension. Since the completeness level strongly depends on the stellar magnitude, we evaluated C considering only simulated objects within a 0.5 large magnitude bin, centered on the V-band magnitude of each star. Finally, the uncertainties σ_C on the completeness value of each star were computed by propagating the Poissonian errors. Figure 4 shows the variation of C as a function of the V-band magnitude in a selection of radial bins.

3 MASS FUNCTION

To derive the cluster MF, we first selected as bona-fide cluster members those stars lying along the observed and well-defined main sequence of the two clusters. To this end, we built the cluster mean ridge lines by computing the 3σ -clipped average color of stars within different bins in the magnitude range $18.5 < V < 26$ and $18 < V < 26$ for M15 and M30, respectively. In both cases, we adopted a 0.25 mag bin width and in each bin we selected as bona-fide cluster stars those located within 3σ the measured average color (see black curve in Figure 5). We used isochrones from the

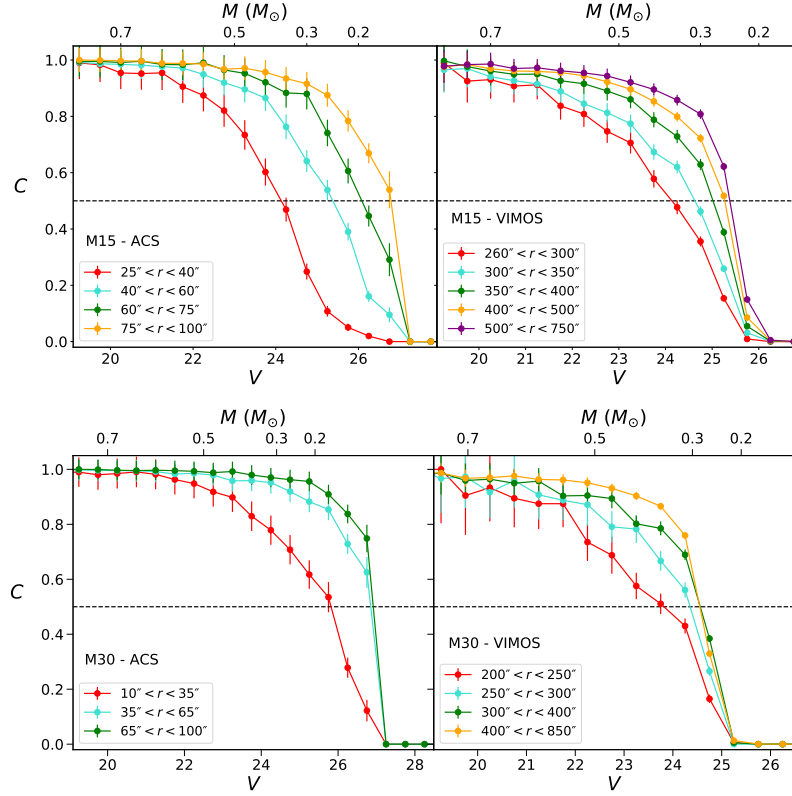


Figure 4. Completeness curves as a function of the V-band magnitudes (stellar mass) for both M15 (top panels) and M30 (bottom panels) and separately shown for the ACS data-set (left panels) and the VIMOS data-set (right panels). Different curves, extracted at different radial distances from the cluster center, are plotted. The dashed horizontal lines mark the lowest completeness level ($C = 0.5$) considered in the data analysis.

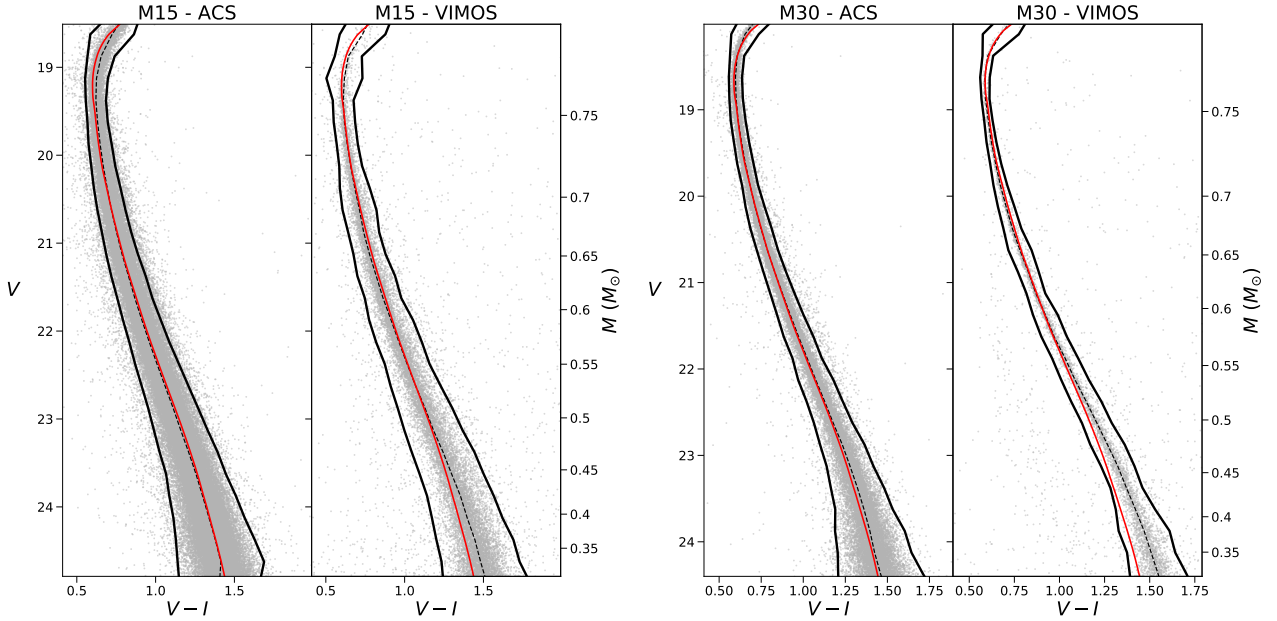


Figure 5. Left panel: CMDs obtained from the ACS and VIMOS data-set of M15. Black curves enclose the selected bona-fide main sequence cluster stars for which we derived the mass. The dashed black curve is the cluster mean-ridge line. The red curve is the adopted isochrone model from which we derive stellar masses at different V-band magnitudes. Right panel: same as in the left panel, but for the case of M30.

Dartmouth Stellar Evolution Database (Dotter et al. 2007) for a stellar population with an age of 13.25 Gyr (Dotter et al. 2010) and with a metallicity of $[Fe/H] = -2.3$ and $[\alpha/Fe] = +0.2$, suitable for both clusters (Carretta et al. 2009; Lovisi et al. 2013). Absolute magnitudes were converted to the observed frame by adopting a distance modulus of $(m - M)_0 = 15.17$ and a color excess of $E(B - V) = 0.08$ in the case of M15, while we adopted a distance modulus of $(m - M)_0 = 14.72$ and a color excess of $E(B - V) = 0.05$ in the case of M30 (Ferraro et al. 1999). Figure 5 shows that the isochrones nicely reproduce the observed CMDs, although a small deviation is visible in the low-luminosity regions of both the clusters' main sequence. This, however, has a negligible effect in the following analysis. We applied an interpolation to derive the masses as a function of the V-band magnitude, as predicted by the isochrone models. As can be seen, both data-sets cover a broad range of masses from $0.76 M_\odot$ (turn-off mass) down to $\sim 0.3 - 0.2 M_\odot$.

To compute the stellar MFs of each cluster, we counted the number of stars located at different distance bins from the cluster center. In order to maximize the reliability of the results, we restricted the analysis only to the stars with completeness larger than 50%. Thus in the case of M15 we considered only stars in the mass range $0.40M_\odot - 0.75M_\odot$ and located only at distances larger than $25''$ and $250''$ from the cluster center of the ACS and VIMOS data-set, respectively. In the case of M30, we considered stars in the same mass range but located at distances larger than $10''$ and $200''$ from the cluster center of the two data-sets. The completeness corrected number of stars and its uncertainty in each radial and mass bin are $N_{corr} = \sum_i^{N_{obs}} C_i^{-1}$ and $\sigma_{N_{corr}} = \sqrt{\sum_i^{N_{obs}} (\sigma_{C_i}/C_i)^2}$, respectively, where N_{obs} is the number of stars observed in a given bin, C_i the completeness of the i^{th} star and σ_{C_i} its uncertainty derived as described in Section 2.1. The MFs evaluated at different radial bins are plotted in Figure 6. The number and widths of the radial bins have been set to sample approximately an equal number of stars, which is 24000 and 8500 for the ACS data-set and 2000 and 900 for the VIMOS data-set of M15 and M30, respectively. To quantify the contamination by field interlopers, we evaluated, in different mass bins, the stellar density in an outer radial bin located at distances larger than $900''$ and $1300''$ from the centers of M15 and M30, respectively, beyond the cluster tidal radii (see Table 1). Then, in each radial and mass bin we subtracted to N_{corr} the completeness corrected number of interlopers expected on the basis of the bin area and of the measured stellar density in the outer bin. Results of this analysis are shown in Figure 6. As expected, the MF slopes decrease significantly moving from the cluster centers to the outskirts.

To quantify the radial variation in the slope of the stellar MFs, we performed a linear fit to each of the measured stellar MFs reported in Figure 6. The resulting slopes are reported in Table 2 and they are plotted as a function of the logarithmic distance from the cluster center expressed in units of half-mass radii r_{hm} in Figure 7. For the 2D projected half-mass radius, r_{hm} , we adopted the values quoted in Table 1. Both clusters show quite similar radial variations of their slopes suggesting a similar dynamical evolution. Indeed, the central regions covered by the HST data-set are characterized by a rapidly steepening of the slopes for increasing clus-

tercentric distances. Such a trend is the expected outcome of the mass segregation process. On the other hand, the cluster outskirts, mapped through the VIMOS data-set, are characterized by nearly constant slopes that can be explained as the combined effect of mass segregation and preferential loss of low-mass stars in the external region of both clusters due to the interaction with the Galaxy potential.

3.1 Main sources of uncertainties

In the following we discuss three potential sources of uncertainties and their impact on the derived MFs. These are: the uncertainties on the photometric completeness assigned to each star, the accuracy on the assignment of stellar masses along the main-sequence and, finally, the role of binaries.

- To assess the impact of the photometric completeness uncertainties in the derivation of the MF slopes, we repeated several times, for each radial bin, the derivation of the MFs as described above. During each iteration, the completeness of each star was randomly drawn from a normal distribution centered on its completeness level and with a standard deviation equal to its uncertainty. At the end of the procedure, we obtained the MF slope distributions and we computed their 16th, 50th and 84th percentiles to quantify the spread introduced by the completeness uncertainties. Such a spread turned out to be as large as ~ 0.005 , thus negligible with respect to the uncertainties quoted in Table 2 and due to the residuals of the linear fit of the MFs.

- The results here obtained are based on the stellar masses derived through the mass-luminosity relation predicted by the Dotter et al. (2007) isochrones. Different models differing in terms of various assumption about stellar evolution, underlying chemical mixture and bolometric corrections could lead to slightly different mass-luminosity relation. To quantify the effect this may have on the derived MF slopes, we repeated the whole analysis deriving the stellar masses using isochrones generated from the Victoria-Regina Isochrone Database (VandenBerg et al. 2014), the BaSTI stellar evolution models (Pietrinferni et al. 2004, 2006) and the PARSEC database (Marigo, et al. 2017). For each of these databases, we extracted an isochrone with the same stellar age and metallicity used before. Results for both clusters show basically no differences in the radial variation of the MF slopes ($\delta\alpha$, see Section 4). Also, the global MF slopes α_G obtained using the Victoria-Regina isochrone are basically the same as derived with the Dartmouth Stellar Evolution model. On the contrary, the α_G values obtained by using the BaSTI and PARSEC models turned out to give systematically flatter MFs (up to $\delta\alpha \sim 0.5$) than those reported in Table 2.

- Finally, to evaluate the impact of binaries, we repeated the analysis selecting only the stars in the blue side of the mean ridge lines shown in Figure 5. This region is in fact expected to be populated almost exclusively by single stars. The general results are unchanged and deviations from the values quoted in Table 2 are $\lesssim 15\%$. Therefore binary systems do not have a significant impact on our analysis. Indeed, both cluster's host a small binary fraction ($\sim 2 - 3\%$; Milone, et al. 2012) that is likely centrally segregated due to the advanced stage of dynamical evolution of both the systems.

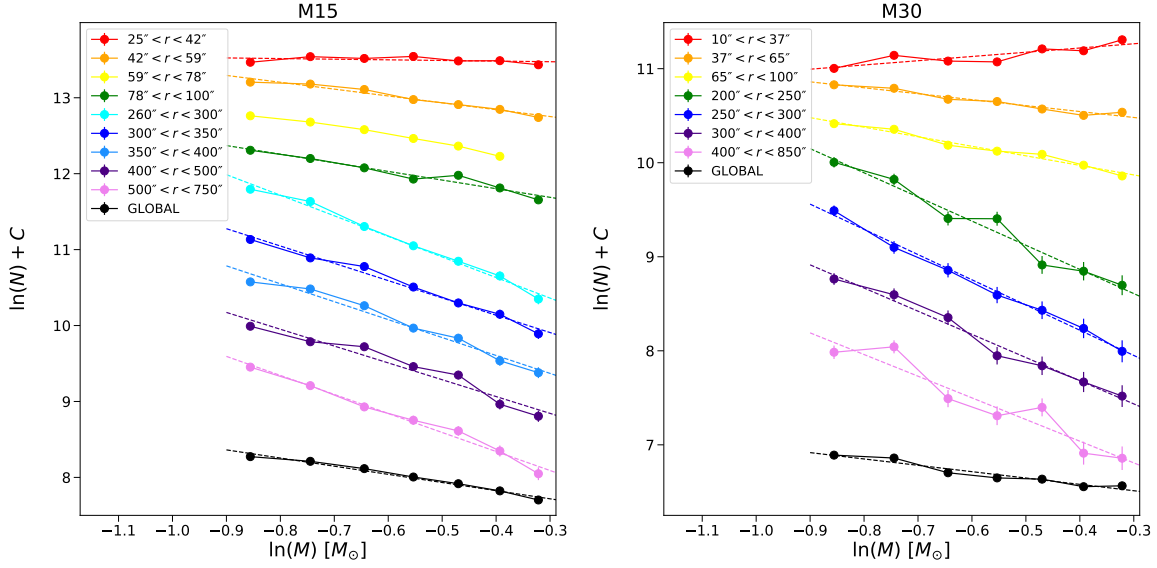


Figure 6. *Left Panel:* Stellar MFs obtained from the M15 data-set used in this work. Different colors correspond to different radial bins, as specified in the legend. An arbitrary constant was added to the different MFs for clarity. The lines represent the linear best fit obtained for each of the MFs. *Right Panel:* same but for the case of M30.

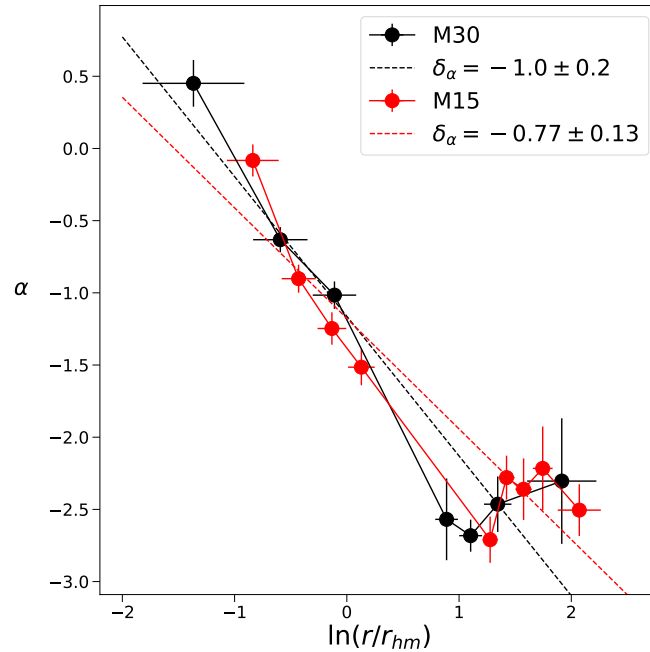


Figure 7. Variation of the slope of the MF with respect to the logarithmic distance from the cluster center expressed in units of half-light radii. The dashed lines are the best linear fit to the observed slope variations and their slopes δ_α are reported in the legend. Black and red points and lines are for M30 and M15, respectively.

4 COMPARISON TO N -BODY SIMULATIONS

4.1 The N -body simulation set

For a more quantitative interpretation of the observational results, we will compare them to N -body simulations from Webb & Vesperini (2016) that model the evolution of star clusters in a Milky Way-like external tidal field. The simulations were performed using the direct N -body code NBODY6 (Aarseth 2003), with each star cluster's initial

conditions generated assuming a Plummer density profiles (Plummer 1911) out to a cutoff of ten half-mass radii. In order to consider both initially compact and extended clusters, we will be comparing the observations to model clusters with initial half-mass radii $r_{hm,i}$ of 1.2 and 6 pc.

Both model clusters initially consists of 10^5 stars, with masses drawn from a Kroupa, Tout & Gilmore (1993) IMF in the range 0.1 - $50 M_\odot$. Hence their initial masses are

Table 2. Slopes of the stellar MFs derived at different distances r from the cluster centers.

M15		M30	
r''	α	r''	α
25-42	-0.08 ± 0.11	10-37	0.45 ± 0.16
42-59	-0.90 ± 0.10	37-65	-0.63 ± 0.09
59-78	-1.25 ± 0.11	65-100	-1.02 ± 0.10
78-100	-1.52 ± 0.13	200-250	-2.6 ± 0.3
260-300	-2.71 ± 0.16	250-300	-2.7 ± 0.1
300-350	-2.28 ± 0.15	300-400	-2.5 ± 0.2
350-400	-2.4 ± 0.2	400-850	-2.3 ± 0.4
400-500	-2.2 ± 0.3	GLOBAL	-0.68 ± 0.10
500-750	-2.51 ± 0.18		
GLOBAL	-1.07 ± 0.08		

approximately $6 \times 10^4 M_\odot$. Stars then evolve with time according to the stellar evolution algorithms of Hurley et al. (2000) assuming a metallicity $Z = 0.001$.

The Milky Way-like potential within which both clusters are evolved is made up of a point-mass bulge, a Miyamoto & Nagai (1975) disk, and logarithmic halo. The bulge has a mass of $1.5 \times 10^{10} M_\odot$ while the disk has a mass of $5 \times 10^{10} M_\odot$ and scale radii of $a = 4.5$ kpc and $b = 0.5$ kpc. The logarithmic halo is scaled such that all three components combine to yield a circular velocity of 220 km/s at 8.5 kpc. Both model clusters have circular orbits at 6 kpc from the center.

4.2 Comparing models and observations

In measuring the radial variation of the simulated cluster's MFs, we project the positions of each stars onto a random two-dimensional plane and only include stars in the same mass range and fields of view as our observed data-set. For each observed cluster, we have determined the boundaries of the fields of view in terms of the cluster's half-mass radius. These boundaries are then used to determine what subset of stars in each N-body simulation should be considered when measuring the MF and its radial variation, with the half-mass radius of the cluster at the current time-step being used to scale the boundaries. Following Webb et al. (2017) we present the cluster evolution in terms of the linear slope of the radial variation of the MF slopes, defined as: $\delta_\alpha = d\alpha(r)/d \ln(r/r_{hm})$, which is a good measure of a GC's degree of mass-segregation, and the slope of the global MF α_G , which is a proxy of the mass lost by a cluster (Vesperini & Heggie 1997; Webb & Leigh 2015), with respect to the ratio between the cluster stellar age and its current half-mass relaxation time t/t_{rh} .

First of all, we measured δ_α and α_G for both clusters. α_G was measured by counting all the stars in a single radial bin covering the entire radial extension considered for the local α measurements (see Table 2 and Figure 7), thus in regions where the completeness is always larger than 50%. Please note that, due to the field of view geometry (see Figure 1), the outer radial bins cover smaller radial extensions than the inner ones and by consequence the latter have a larger weight in the derived α_G values. Therefore extra-caution should be used when comparing the values here derived with those obtained using different data-sets.. We found $\delta_\alpha = -0.77 \pm 0.13$ and $\alpha_G = -1.07 \pm 0.08$ for the case of M15, while we found $\delta_\alpha = -1.0 \pm 0.2$ and $\alpha_G = -0.68 \pm 0.10$

for the case of M30. While this is the first time that δ_α is measured for these two clusters, we can compare the α_G values here derived with those quoted in previous works. Paust, et al. (2010) found $\alpha_G = -0.92 \pm 0.06$ for M30, while no values is reported for M15. Sollima & Baumgardt (2017) found instead $\alpha_G = -1.16 \pm 0.06$ and $\alpha_G = -0.72 \pm 0.02$ for M15 and M30, respectively, while Ebrahimi et al. (2020) report $\alpha_G = -1.00 \pm 0.04$ and $\alpha_G = -0.80 \pm 0.03$ for M15 and M30, respectively. Finally, the compilation of Baumgardt, & Hilker (2018) quotes $\alpha_G = -0.53$ and $\alpha_G = -1.02$ for M15 and M30, respectively. Therefore, there is a general reasonable agreement between our and previous works. However, we stress that all these literature values were obtained through a combination of observations and modelling, and, for the values reported in Baumgardt, & Hilker (2018), also considering stars in a mass range slightly different than that adopted in this work. On the other hand, our results are based exclusively on observations, although the outer regions are not uniformly sampled and thus the α_G values are likely biased toward the inner regions of the cluster.

To evaluate the ratio t/t_{rh} , we adopted $t = 13.25 \pm 0.75$ Gyr for both the clusters (Dotter et al. 2010), while we derived t_{rh} following Spitzer & Hart (1971):

$$t_{rh} = 2.054 \times 10^6 \text{ yr} \frac{M^{\frac{1}{2}}}{\langle m \rangle} \frac{r_{hm}^{\frac{3}{2}}}{\ln(0.4 \frac{M}{\langle m \rangle})}$$

where M is the cluster's mass in units of solar masses, r_{hm} is the projected half-mass radius (see Table 1) in pc units and $\langle m \rangle$ is the mean stellar mass (assumed to be, as in the Harris 2010 catalog, $\frac{1}{3} M_\odot$). We found $t_{rh} = 2.5 \pm 0.5$ Gyr for M15 and $t_{rh} = 1.3 \pm 0.3$ Gyr for M30, thus implying $t/t_{rh} = 5.3 \pm 1.1$ and $t/t_{rh} = 10 \pm 2$ for M15 and M30, respectively.

4.3 M15

In the left panel of Figure 8, we show the model cluster evolution in the $(\delta_\alpha, \alpha_G)$ plane, together with the measured positions of M15 in this parameter space. A nice match is reached with both the extended and compact cluster simulations. However, we note that M15 falls in a region of this diagram in which the expected evolution of δ_α is largely insensitive to α_G variations. This is essentially due to the fact that δ_α stops decreasing since segregation in the core has stopped and tidal stripping in the outer regions prevents α from decreasing further. However, the global α will continue to increase as low-mass stars escape the cluster. For this reason we also compared the behavior of both δ_α and α_G with respect to t/t_{rh} . The middle and right panels of Figure 8 show that while the observed value of δ_α is well reproduced by the models at the estimated t/t_{rh} , α_G is significantly flatter than predicted. Indeed, at the cluster corresponding t/t_{rh} , the models predict an α_G value around -1.6 for the extended cluster and around -2 for the compact one. The model is able to match the observed α_G value only at significantly later stages of the evolution, around $t/t_{rh} \sim 30$, which is a factor of 3 larger than what estimated for M15. Any reasonable uncertainties on both age and relaxation time would be hardly able to account for such a large difference. It is also important to note that had we used the α_G values derived adopting other isochrones (see

Section 3.1), the discrepancy between observations and simulations would have been even more severe.

The flatter α_G found in our observational data would suggest that M15 has lost significantly more mass than predicted by our simulations. However, the strength of the external tidal field adopted in the simulations is similar to that inferred from the orbit of M15 (which is currently on a slightly eccentric orbit at a Galactocentric distances around 4–10 kpc; Baumgardt et al. 2019). In addition, as shown in Webb & Vesperini (2016), the dependence of the evolution of both δ_α and α_G on the orbital properties is not sufficient to explain the observed discrepancy. Exceptional events, such as tidal shocks or interactions with molecular clouds, that could increase the mass-loss rate over a relatively short period of time, are not taken into account by the models. However, these are rare events that are unlikely to explain the observed discrepancy. In any case, further simulations are needed to firmly confirm the effects of such events in the evolution of both the radial and global MF slopes. As far as the possible effects of primordial mass segregations are concerned, Webb & Vesperini (2016) have shown that for old GCs and the mass range considered in this study a broad range of different degrees of primordial mass segregation do not have a strong effect on the value of α_G after one Hubble time. Finally, our two simulations cover a broad range of initial half-mass radii and given the variation of the evolution of δ_α and α_G with this parameter, it is unlikely that the observed discrepancy could be explained by a different choice for the initial half-mass radius.

A different IMF, flatter than the Kroupa, Tout & Gilmore (1993) IMF adopted here could easily remove the difference between observations and models, as this cluster would start the evolution with a larger value of α_G . Our analysis thus suggests that a different IMF might be the most likely explanation to the observed (α_G , δ_α , t/t_{rh}) trends.

4.4 M30

Figure 9 shows the same diagnostic plots we used for M15 but for the case of M30. Also in this case the derived values of (δ_α , α_G) are nicely reproduced by the simulations. However, as in the case of M15, the simulations are not able to match the observations in the (α_G , t/t_{rh}) diagram where actually the discrepancy is even larger than for M15. The α_G value measured for M30 is reached by the simulations at a very late stages of the evolution, around $t/t_{rh} \sim 40$, significantly larger than the value of this ratio determined from observational data. Also in this case, the derivation of α_G assuming different stellar evolution models (see Section 3.1) would further increase the mismatch.

The same arguments discussed for M15 also apply to M30. One difference to note is that M30 has a very eccentric orbit in a distance range $\sim 1.5 - 8$ kpc from the Galaxy center, thus with a pericenter smaller than the distance adopted in our simulations. However, again, the dependence on the cluster's orbit (see Webb & Vesperini 2016) is unlikely to account for the differences between observational data and numerical models revealed by our analysis. In any case, given the differences between the real and simulated orbits, the discrepancy could be partially due to a larger degree of mass-loss due to the cluster highly eccentric orbit. It also worth mentioning that, on the basis of its current orbit, Massari et

al. (2019) suggested that M30 formed in the Gaia-Enceladus dwarf galaxy. This would mean that M30 could have experienced a milder tidal field than in the Galaxy, during the early stage of its evolution. However, this should not have a significant impact in our analysis, since the merger event with the dwarf Gaia-Enceladus dates back to ~ 10 Gyr ago (Kruijssen, et al. 2020) and therefore the cluster spent most of its life in the Milky Way. *Given all this, we suggest that also for this cluster a different, flatter/bottom-lighter, IMF is likely to be required to reconcile observational data with theoretical models.*

5 CONCLUSIONS AND DISCUSSION

We used a combination of deep, high-resolution and wide-field optical observations of the dynamically old Galactic GCs M15 and M30 to investigate their dynamical evolution in terms of the radial variation of their stellar MF along the whole cluster radial extensions. Both clusters reveal a quite similar variation of the MF slopes with respect to the clustercentric distance. In fact, the inner regions (approximately within r_{hm}) show a progressive steepening of the MF slopes while moving away from the cluster centers. On the other hand, the outer regions (approximately from $5r_{hm}$ to their tidal radii) are characterized by almost constant MF slopes. This trend is the expected outcome of the long-term dynamical evolution driven by two-body encounters and progressive mass-loss due to the cluster interactions with the Galaxy.

We compared the observed results with a set of direct N -body models, following the cluster evolution in a Milky Way-like potential, assuming a standard Kroupa, Tout & Gilmore (1993) IMF. Such a comparison has been performed by means of two powerful indicators of the cluster degree of mass-segregation and mass-loss: the radial variation of the MF slope (δ_α) and the slope of the global MF (α_G), respectively. We found that the models are able to nicely reproduce the measured values in the (δ_α , α_G) diagram. However, in both M15 and M30, the dynamical state of the cluster as traced by the (δ_α , t/t_{rh}) and (α_G , t/t_{rh}) is reproduced only at significantly later stages of the evolution, when the ratio between the cluster age to the instantaneous half-mass relaxation time is $\sim 3 - 4$ times larger than the measured ratios for the two clusters. As largely discussed in Webb & Vesperini (2016), different assumptions about the initial binary fractions and dark remnants (and their retention), as well as on the cluster's orbit cannot account for such a differences. On the other hand, also the uncertainties on the observed quantities cannot explain the discrepancy between observations and simulations.. The results obtained in this paper would suggest that the most likely explanation to such a significant discrepancy is the adoption of a non universal IMF, flatter/bottom-lighter than the one assumed by models.

A correlation between the global MF slopes and the half-mass relaxation time (and the ratio of the age to the half-mass relaxation time) of a sample of Galactic GCs, with dynamically older clusters showing flatter MF slopes, was recently found by Sollima & Baumgardt (2017) and Ebrahimi et al. (2020). Such a correlation may be difficult to reconcile with significant variations of the IMF and it has been argued it is likely to result from the effects the dynamical

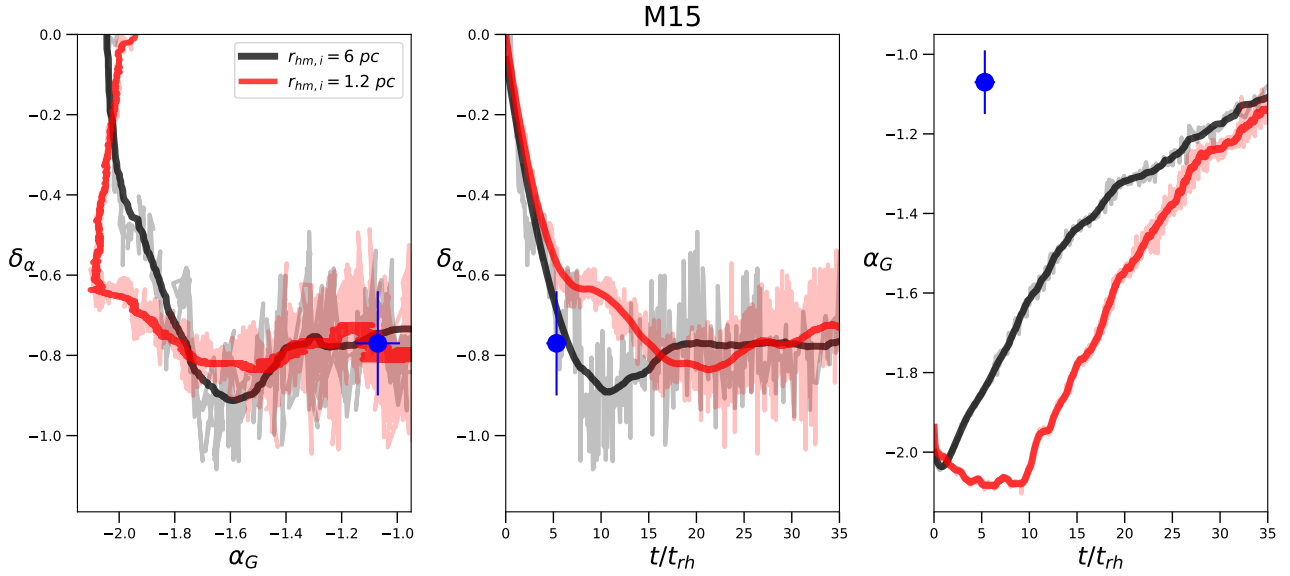


Figure 8. The left panel shows the evolution of slope of the best linear fit to the observed variation in the slope of the stellar MF (δ_α) with respect to the slope of the global MF (α_G). The middle and right panels show instead the evolution of δ_α and α_G with respect to the ratio between the cluster age and the instantaneous half-mass relaxation time (t/t_{rh}). The red and black lines correspond to the smoothed evolution of direct N -body star cluster simulations with initial half-mass radii of 1.2 pc and 6 pc. The shaded areas show instead the real values of the simulations. For comparison purposes, the blue points mark the positions of M15 in this parameter space.

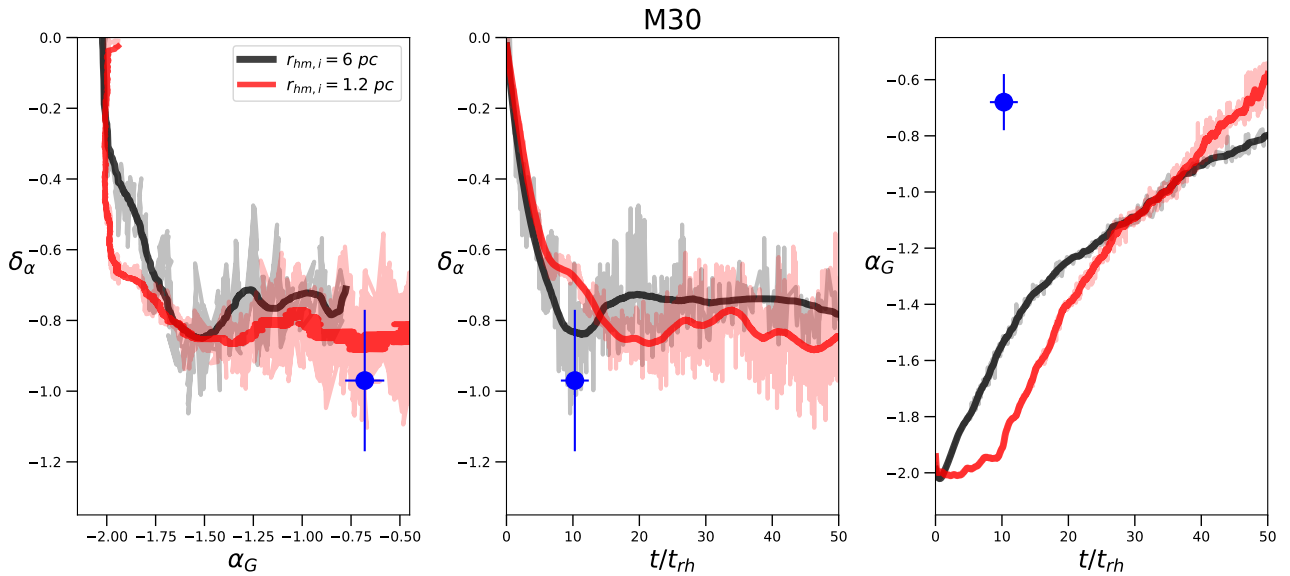


Figure 9. As in Figure 8, but for the case of M30.

evolution alone. However, the situation appears to be more complicated and the presence of IMF variations cannot be excluded. In general, the star forming environment should play an important role in shaping the IMF of stellar systems (see e.g. [Silk 1977](#); [Strader et al. 2011](#); [Giersz & Heggie 2011](#); [Hénault-Brunet, et al. 2020](#); [Ebrahimi et al. 2020](#); [Kroupa 2020](#), for some theoretical and observational studies about this topic). In this respect, it is important to point out that other studies have noted that the discrepancy between theoretical predictions and observations of metal-rich GC

mass-to-light ratios might be due to a non-standard IMF, either bottom-light (i.e. fewer low-mass stars) or top-light MFs (i.e. fewer dark remnants) (see [Strader et al. 2011](#) and [Hénault-Brunet, et al. 2020](#), in which other possibilities in alternative to a non-universal IMF are also discussed). The results obtained in this work would suggest possible IMF variation also at very metal-poor regime.

One aspect that has not been investigated yet, neither theoretically nor observationally, concerns the possible variations in the IMF of multiple stellar populations observed in

almost all Galactic GCs. Different observations suggest that the chemically anomalous second population (i.e. Na-rich, O-poor) of stars form in a compact system more segregated with respect to the first population of stars (see [Lardo et al. 2011](#); [Dalessandro et al. 2019](#)) as predicted by multiple population formation scenarios (see [Bastian & Lardo 2018](#); [Gratton et al. 2019](#) for recent reviews). The implications of the different formation environments of stars in the first and second populations are still unknown and the connection with the possible evidence of a non universal IMF will require further studies.

More in general, constraining the IMF of stellar clusters have key implications on our understanding of their formation process and early evolution, with strong impact on the early enrichment undergone by stellar clusters, gas consumption efficiency, stellar cluster initial mass and their contribution to building-up of the Galactic halo.

ACKNOWLEDGEMENTS

The authors thank the anonymous referee for the careful reading of the paper and the constructive comments. We also thank B. Lanzoni for useful discussion. MC and ED acknowledge financial support by the project Light-on-Dark granted by MIUR through PRIN2017-000000 contract.

Based on observations collected at the European Southern Observatory under ESO programme 097.D-0145(A).

Based on observations made with the NASA/ESA Hubble Space Telescope, obtained from the Data Archive at the Space Telescope Science Institute, which is operated by the Association of Universities for Research in Astronomy, Inc., under NASA contract NAS 5–26555. These observations are associated with program GO 10755.

The data underlying this article will be shared on reasonable request to the corresponding author.

REFERENCES

- Aarseth, S. J. 2003, *Gravitational N-Body Simulations*
- Anderson, J., Sarajedini, A., Bedin, L. R., et al. 2008, *AJ*, 135, 2055
- Bastian, N., & Lardo, C. 2018, *ARA&A*, 56, 83
- Baumgardt, H., & Makino, J. 2003, *MNRAS*, 340, 227
- Baumgardt, H., & Hilker, M. 2018, *MNRAS*, 478, 1520
- Baumgardt, H., Hilker, M., Sollima, A., et al. 2019, *MNRAS*, 482, 5138
- Beccari, G., Sollima, A., Ferraro, F. R., et al. 2011, *ApJ*, 737, L3
- Beccari, G., Ferraro, F. R., Dalessandro, E., et al. 2019, *ApJ*, 876, 87
- Bellazzini, M., Fusi Pecci, F., Messineo, M., Monaco, L., & Rood, R. T. 2002, *AJ*, 123, 1509
- Cadelano, M., Pallanca, C., Ferraro, F. R., et al. 2015, *ApJ*, 812, 63
- Cadelano, M., Ransom, S. M., Freire, P. C. C., et al. 2018, *ApJ*, 855, 125
- Cadelano, M., Ferraro, F. R., Istrate, A. G., et al. 2019, *ApJ*, 875, 25
- Carretta, E., Bragaglia, A., Gratton, R., et al. 2009, *A&A*, 508, 695
- Dalessandro, E., Beccari, G., Lanzoni, B., et al. 2009, *ApJS*, 182, 509
- Dalessandro, E., Lanzoni, B., Beccari, G., et al. 2011, *ApJ*, 743, 11
- Dalessandro, E., Ferraro, F. R., Massari, D., et al. 2013, *ApJ*, 778, 135
- Dalessandro, E., Ferraro, F. R., Massari, D., et al. 2015, *ApJ*, 810, 40
- Dalessandro, E., Cadelano, M., Vesperini, E., et al. 2018, *ApJ*, 859, 15
- Dalessandro, E., Cadelano, M., Vesperini, E., et al. 2019, *ApJ*, 884, L24
- Dotter, A., Chaboyer, B., Jevremović, D., et al. 2007, *AJ*, 134, 376
- Dotter, A., Sarajedini, A., Anderson, J., et al. 2010, *ApJ*, 708, 698
- Ebrahimi, H., Sollima, A., Haghi, H., et al. 2020, *MNRAS*, 494, 4226
- Ferraro, F. R., Messineo, M., Fusi Pecci, F., et al. 1999, *AJ*, 118, 1738
- Ferraro, F. R., Beccari, G., Dalessandro, E., et al. 2009, *Nature*, 462, 1028
- Ferraro, F. R., Lanzoni, B., Dalessandro, E., et al. 2012, *Nature*, 492, 393
- Ferraro, F. R., Lanzoni, B., Raso, S., et al. 2018, *ApJ*, 860, 36
- Gaia Collaboration, Brown, A. G. A., Vallenari, A., et al. 2018, *A&A*, 616, A1
- Gieles, M., Larsen, S. S., Bastian, N., et al. 2006, *A&A*, 450, 129
- Giersz, M., & Heggie, D. C. 2011, *MNRAS*, 410, 2698
- Gratton, R., Bragaglia, A., Carretta, E., et al. 2019, *A&ARv*, 27, 8
- Harris, W. E. 2010, *arXiv e-prints*, arXiv:1012.3224
- Heggie, D., & Hut, P. 2003, *The Gravitational Million-Body Problem: A Multidisciplinary Approach to Star Cluster Dynamics*
- Hénault-Brunet V., Gieles M., Strader J., Peuten M., Balbinot E., Douglas K. E. K., 2020, *MNRAS*, 491, 113
- Hurley, J. R., Pols, O. R., & Tout, C. A. 2000, *MNRAS*, 315, 543
- Kains, N., Bramich, D. M., Arellano Ferro, A., et al. 2013, *A&A*, 555, A36
- Kroupa P., Tout C. A., Gilmore G., 1993, *MNRAS*, 262, 545
- Kroupa P., 2020, *IAUS*, 351, 117, *IAUS*.351
- Kruijssen, J. M. D., Pelupessy, F. I., Lamers, H. J. G. L. M., et al. 2011, *MNRAS*, 414, 1339
- Kruijssen, J. M. D., Maschberger, T., Moeckel, N., et al. 2012, *MNRAS*, 419, 841
- Kruijssen J. M. D., et al., 2020, *arXiv*, arXiv:2003.01119
- Li, H., & Gnedin, O. 2019, *arXiv e-prints*, arXiv:1908.00984
- Lanzoni, B., Dalessandro, E., Perina, S., et al. 2007, *ApJ*, 670, 1065
- Lanzoni, B., Ferraro, F. R., Alessandrini, E., et al. 2016, *ApJ*, 833, L29
- Lardo, C., Bellazzini, M., Pancino, E., et al. 2011, *A&A*, 525, A114
- Lovisi, L., Mucciarelli, A., Lanzoni, B., et al. 2013, *ApJ*, 772, 148
- Mamikonian, E. N., McMillan, S. L. W., Vesperini, E., et al. 2017, *ApJ*, 837, 70
- Marigo P., et al., 2017, *ApJ*, 835, 77
- Massari, D., Koppelman, H. H., & Helmi, A. 2019, *A&A*, 630, L4
- Meylan, G., & Heggie, D. C. 1997, *A&ARv*, 8, 1
- Milone A. P., et al., 2012, *A&A*, 540, A16
- Miyamoto, M., & Nagai, R. 1975, *PASJ*, 27, 533
- Noyola, E., & Gebhardt, K. 2006, *AJ*, 132, 447
- Paust N. E. Q., et al., 2010, *AJ*, 139, 476
- Pietrinferni, A., Cassisi, S., Salaris, M., et al. 2004, *ApJ*, 612, 168
- Pietrinferni, A., Cassisi, S., Salaris, M., et al. 2006, *ApJ*, 642, 797
- Plummer, H. C. 1911, *MNRAS*, 71, 460
- Renaud, F., & Gieles, M. 2013, *MNRAS*, 431, L83
- Rieder, S., Ishiyama, T., Langelaan, P., et al. 2013, *MNRAS*, 436, 3695
- Sarajedini, A., Bedin, L. R., Chaboyer, B., et al. 2007, *AJ*, 133, 1658
- Shanahan, R. L., & Gieles, M. 2015, *MNRAS*, 448, L94

- Silk, J. 1977, *ApJ*, 214, 718
 Simunovic, M., Puzia, T. H., & Sills, A. 2014, *ApJ*, 795, L10
 Sollima A., Baumgardt H., 2017, *MNRAS*, 471, 3668
 Spitzer, L., & Hart, M. H. 1971, *ApJ*, 164, 399
 Stetson, P. B. 1987, *PASP*, 99, 191
 Stetson, P. B. 1994, *PASP*, 106, 250
 Stetson, P. B., Pancino, E., Zocchi, A., et al. 2019, *MNRAS*, 485, 3042
 Strader, J., Caldwell, N., & Seth, A. C. 2011, *AJ*, 142, 8
 VandenBerg, D. A., Bergbusch, P. A., Ferguson, J. W., & Edvardsson, B. 2014, *ApJ*, 794, 72
 Vesperini, E., & Heggie, D. C. 1997, *MNRAS*, 289, 898
 Webb J. J., Leigh N. W. C., 2015, *MNRAS*, 453, 3278
 Webb, J. J., & Vesperini, E. 2016, *MNRAS*, 463, 2383
 Webb, J. J., Vesperini, E., Dalessandro, E., et al. 2017, *MNRAS*, 471, 3845

This paper has been typeset from a \LaTeX file prepared by the author.